# Design and Analysis of an Outer Mover Linear-Rotary Vernier Machine

**Abstract** – According to the requirements of large torque and high precision linear displacement of the drilling robot, an outer mover (OM) linear-rotary (LR) vernier machine (VM) is proposed with a special support mechanism, which combines an outer rotor VM and a cylindrical OM linear VM. In order to reduce the detent force and improve the displacement accuracy of the linear motion when the proposed motor works at low speed and short stroke conditions, the modular stators and permanent magnet poles are adopted instead of the traditional toroid structure. Since the torque is the main output quantity and the linear motion mainly determines the linear displacement, the design of the rotary unit is taken as the optimization objective firstly. Then, the cogging torque and detent force of OMLRVM are added to the optimization objectives. The electromagnetic and mechanical designs of the proposed motor are calculated based on 3-D finite element model. Compared with the results of the initial topologies I and II, the end effects of rotary and linear units are reduced thanks to the support mechanism, and the amplitudes of cogging torque and detent force are decreased. The idea of combined electromagnetic and mechanical design is an effective way to solve the practical application problems in industrial field.

## 1. Introduction

The main problem of drilling robot technology research is to control the position and depth of drilling hole precisely, which can affect the drilling efficiency and precision. Linear-rotary machine (LRM) with high response speed is the optimum choice to solve the problem, and the research of LRM is concerned by many scholars. Vernier machine (VM) can generate high torque density, and it is widely used in industrial field, especially in the last few years. In [1], a linear permanent magnet (PM) VM with V-shaped consequent pole was investigated, and it can increase the air-gap flux density, thrust density, efficiency and power factor. The optimization design of a linear PMVM with highly desired fault-tolerant capability was analyzed by multi-objective optimization method and equivalent magnetic network method in [2] and [3], respectively. The isolation of a PMVM with modular winding was analyzed between phases and modules in [4]. A multi-harmonics linear PMVM was investigated with non-uniformly distributed PM arrays, and its richer harmonics made its performance superior to the traditional linear PMVM [5]. The force ripple reduction principle of a fractional pole-pair linear PMVM was given in [6], which exhibits high back electromotive force (EMF) symmetry and low thrust ripple. A relieving direct current (DC) saturation hybrid excitation VM was introduced in [7], and it can construct the reluctance effect introduced by the DC field excitation, and

integrate high torque density and bidirectional flux control function. A consequent pole PMVM was proposed with dual-sided stator and dual rotor in [8], which has high efficiency and low torque ripple. The scaling effect focused on back EMF of three different power ratings surface-mounted PMVM was analyzed in [9].

The performances and principles of a spoke array PMVM and a linear PMVM were analyzed by the subdomain method and analytical method in [10] and [11], respectively. The power factor, torque and fault tolerant performance of PMVM were investigated based on permeance and equivalent magnetic circuit models [12]. A harmonic reference frame of DC-biased vernier reluctance machines (VRM) was proposed based on harmonic current suppression strategy [13]. Air-gap permeance harmonics of PMVM with coding-shaped tooth were proposed, which can introduce permeance harmonics with specific phase and amplitude, and the electromagnetic performances of the machines were studied by semi-analytical way and finite element methods (FEM) [14]. A new armature winding design method for VRM with DC field coils across two stator teeth was presented based on the flux modulation effect of fundamental DC field harmonic [15]. In order to improve the flux regulation capability and power factor, a dual-stator hybrid excited PMVM was proposed with consequent-pole Halbach-array PMs [16]. A VRM with half-quasi-squirrel cage winding, DC-biased current and ladder rotor was presented, which has high power density and efficiency [17]. A consequent-pole modular mover linear PMVM with dual-flux-modulation effect was proposed and analyzed by FEM in [18]. An axially magnetized PMVM was proposed, which has alternately

magnetized direction PMs clamped on the ends of the rotor [19]. The performance of PMVM was proposed and analyzed by a hybrid analytical model combining subdomain model and equivalent magnetic network, which can consider the saturation effect [20]. A claw pole PMVM was investigated with spoke array PM, which can enhance the magnetic flux modulation effects, and its electromagnetic performances were analyzed by the equivalent circuit analysis and FEM [21]. Overall, the characteristics of the VM have been widely studied.

In order to meet the demand of linear-rotary motion, many linear rotary motors have been presented. The control system and optimization design of linear rotary PM synchronous actuators were analyzed in [22-24]. A rotary and linear motion switched reluctance motor with modular stators was investigated and analyzed by numerical field computation method [25]. A single air-gap LR PM voice coil motor was proposed, and the distributions of the thrust and torque are analyzed by magnetic equivalent circuit method [26]. A rotary linear machine with magnetic bearings was presented and the functions for the torque, thrust and magnetic bearing force were derived in [27]. The performance and parameters of the rotary linear switched reluctance motor were obtained by the analytical method and FEM [28]. The high speed and dynamic response of a linear rotary electromagnetic actuator was achieved by adopting the light weight moving coil [29]. The optimization design of a double stator linear-rotary PM generator with Halbach PM array was analyzed by the operating domain design and non-dominated sorting genetic algorithm II [30]. The helical motion coupling effect of two-degree-of-freedom induction machine and the optimization design of a linear-rotary PM generator with E-shaped stator were analyzed in [31] and [32], respectively. Based on the motor design experience, the topology of LRM is worth to study deeply, which can improve the operating reliability and stability of the control system of linear rotary motion.

In order to accurately control the position and depth of drilling hole, a two degree of freedom (2-DOF) outer mover linear-rotary vernier machine (OMLRVM) is proposed with an outer rotor (OR) VM and a cylindrical outer mover linear VM (OMLVM), which are combined by a support mechanism. The loss, power, efficiency, and volume of ORVM are calculated for determining the circumferential and axial dimensions of the rotary unit. In order to reduce the detent force and improve the linear position accuracy, the modular stator sections and PM poles are adopted in the linear unit. The electromagnetic designs and stress situation of OMLRVM are calculated by 3-D finite element method (FEM). Then the main structure parameters of OMLRVM are obtained.

## 2. Topology of OMLRVM

Fig. 1 illustrates the initial topologies of OMLRVM. The

mover of topology I is connected with support plate and shaft, and its end effect is large. The support mechanism is adopted in topology II, which can reduce the end effect effectively. The disc type stator structure is adopted as the linear motion units of the two topologies.
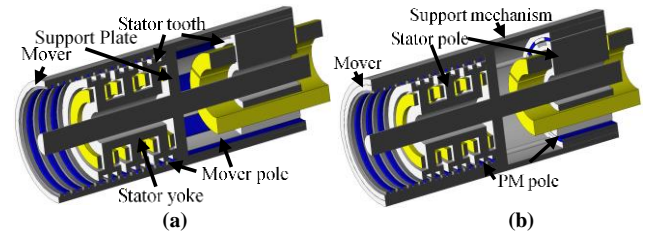


**Fig. 1** Initial topologies of OMLRVM. **a** Topology I, **b** topology II.
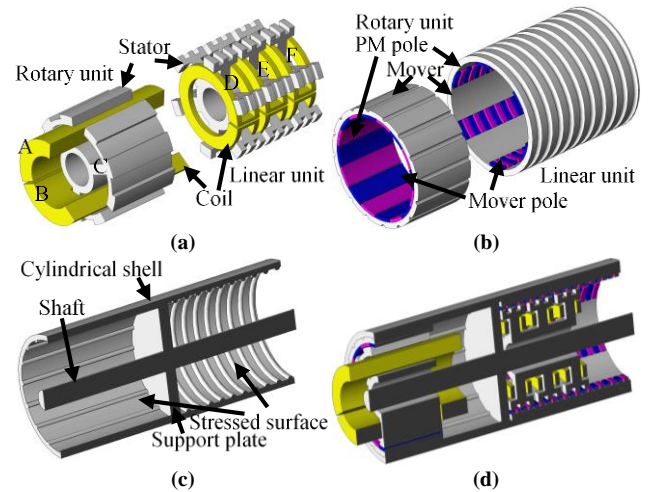


**Fig. 2** Assembly drawing of the proposed OMLRVM. **a** Stator section, **b** mover section, **c** support mechanism, **d** topology.

Fig. 2 illustrates the structural drawing of OMLRVM, which contains the rotary unit, linear unit and a support mechanism. From Fig. 2(c), it is seen that the support plate, cylindrical shell and shaft constitute the support mechanism structure, which does not affect the electromagnetic properties of the proposed motor. In the ORVM structure, the 3/16 pole-slot combination form is adopted. In the OMLVM structure, the traditional disc structure is divided into six stator poles in circumferential direction, which can reduce effectively the detent force and the cost.

Fig. 3 shows the optimization program of OMLRVM. The initial topology is built by 3-D FEM in section II. The main dimensions of OMLRVM are decided by the electromagnetic optimization and mechanical designs in sections III and IV. The iron loss and copper loss, power, efficiency and volume related with the radial and axial radius dimensions of rotary unit are calculated, which is used to select the suitable radial and axial diameters. Then the main dimensions of OMLRVM can be decided. The magnetic field distribution, air-gap flux density, magnetic

flux linkage, torque/thrust and torque/thrust ranges, back EMF and cogging torque/detent force are analyzed in section V.
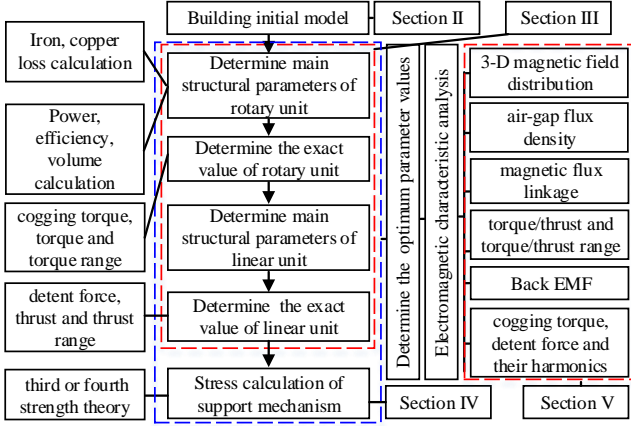


**Fig. 3** Optimization program of OMLRVM.

## 3. Optimization of Electromagnetic Parameters

### 3.1 Operation Principle

When the speed of the magnetic field generated by the current in the armature windings is equal to the speed of that generated by PM material, the torque and thrust can have continuous and smooth output waveform curve. According to the magnetic field calculation modulation of VM in [4-6], the relationship expression of the stator magnetic field pole-pair number generated by armature windings ($P_a$), the main magnetic field pole-pair number generated by PM pole ($P_{PM}$), and the stator teeth number ($Z_s$) of the rotary or linear unit is

$$P_a = | P_{PM} - Z_s | \qquad (1)$$

The expressions of the main PM excited magnetic field velocity ($v_{PM}$) and magnetic gear ratio $G$ of the rotary or linear units are

$$v_{PM} = Gv \qquad (2)$$

$$G = P_a / Z_s \qquad (3)$$

where $v$ is the rotary or linear speed of mover.

Fig. 4 shows the structure parameters of OMLRVM, which can be taken as the optimization variables. $R_{sp1}$, $R_{sp2}$, $R_{sp3}$, $R_{sp4}$ and $R_{sp5}$ are the stator radiuses of rotary unit. $R_{mo}$ and $R_{mi}$ are the outer and inner mover radiuses of rotary unit, respectively. $w_{pm\theta}$, $w_{sp\theta}$ and $\rho_s$ are the widths of PM pole, stator pole and stator tooth, respectively. $R_{sliz}$, $R_{sliz1}$, $R_{sloz1}$, $R_{sloz2}$ and $R_{sloz}$ are the stator radiuses of linear unit. $w_{sppz}$ is the width between stator poles. $w_{spz}$ and $w_{sz}$ are the widths of stator tooth and stator pole, respectively. $w_{sp\theta}$ and $w_{pm\theta}$ are the widths of stator pole and PM pole, respectively. $R_{mlo}$ and $R_{mli}$ are the radiuses of mover, respectively. $w_{gz}$ is the width of air gap between PM poles of linear unit in the axial direction. $w_{pmz}$ is the width of PM pole of the linear

unit in the axial direction. Fig. 5 shows the magnetic flux density distribution of the initial topology. It is seen that the flux density in stator pole is relatively high, and hence the flux density is also an important element for conducting the optimization.
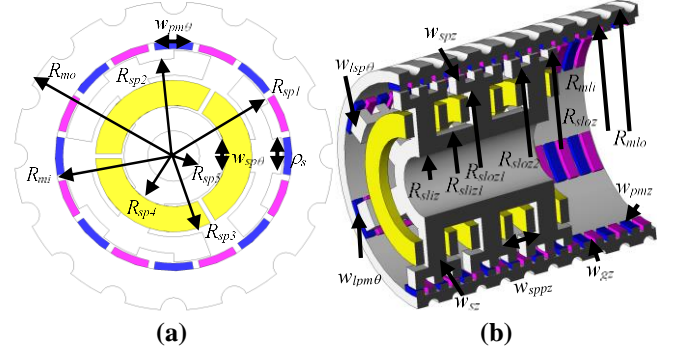

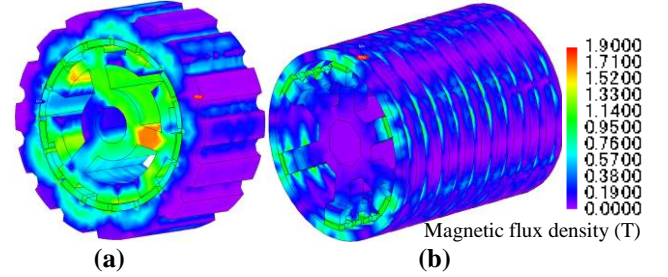
**Fig. 4** The structure of OMLRVM. **a** Rotary unit, **b** linear unit.



**Fig. 5** Magnetic flux density distribution in the initial topology. **a** Rotary unit, **b** linear unit.

### 3.2 Optimization design

Since the torque is the main output quantity and the high precision displacement is achieved by linear motion, the rotary unit is taken as the objective at first, and the method combining analytical calculation method and 3-D FEM is used. Fig. 6 shows the optimization design of electromagnetic characteristics. The optimization of OMLRVM is studied by the method combining analytical calculation and 3-D FEM. 3-D FEM is an effective method to optimize the motor structure, but it costs a lot of time. In the paper, the combined method can reduce the number of finite element simulations and improve optimization efficiency. The computation order of analytical method and FEM are shown in Fig. 6. $h_{pm}$, $g$ and $h_{bl}$ are analyzed by analytical calculation based on the optimization design experience of the traditional surface mounted PM machine. Namely, the parameters $h_{pm}$, $g$, $h_{bl}$ $R_{spl}$, $\rho_s$, $R_{sliz}$, $R_{sliz1}$, $R_{mb}$, $R_{sloz}$, $R_{mli}$, $w_{sppz}$, and $w_{gz}$ are decided by analytical calculation. The parameters $R_{mo}$, z-length, $R_{sp2}$, $R_{sp3}$, $w_{pm\theta}$, $w_{sp\theta}$, $w_{sp4}$, $w_{sp5}$, $h_{bi}$, $w_{pmz}$, $w_{spz}$, $w_{sz}$, $R_{sliz2}$, $R_{sloz1}$, $R_{slz}$, $R_{sliz1}$, $w_{lsp\theta}$ and $w_{lpm\theta}$ can be decided by Figs. 7-13, which are calculated by 3-D FEM.

The height of PM can be decided by

$$h_{pm} = \mu_r \delta_i / (B_r / B_\delta - 1) \qquad (4)$$

where $u_r$ is the relative permeability, $\delta_i$ is the length of air gap, $B_r$ is the radial air gap flux density, and $B_\delta$ is the average air gap flux densities in radial direction. The range of $B_r / B_\delta$ is 1.1~1.35.



**Fig. 6** Optimization design of electromagnetic structure parameters.

The expression of the mover yoke height is

$$h_{bi} = \frac{B_\delta \pi R_{sp1} w_{pm\theta} \, p_\theta / 2\pi}{2B_{bi} p_\theta} = \frac{B_\delta R_{sp1} w_{pm\theta}}{2B_{bi}} \tag{5}$$

where $B_{bi}$ is the flux density in the mover yoke, and $p_\theta$ is the number of pole pairs of rotary unit.

According to (4), (5) and the design experience of PM motor, the values of $h_{PM}$, $g$ and $h_{bi}$ are chosen as 3 mm, 0.6 mm and 12 mm, respectively.



**Fig. 7** Losses of ORVM with different radiuses and axial lengths. **a** Radiuses, **b** axial lengths.

The influence of the armature reaction depends on the rotor magnetic circuit structure. The average effect of armature reaction on the permanent magnet rotor with tile form of radially magnetized permanent magnet is neither demagnetized nor magnetized when the magnetic circuit is not locally saturated at any time in the same state angle range. Then the effect of armature reaction can be ignored, which can be taken as a constant value. From the point of view of the cause of loss, the power loss contains copper loss, iron loss, mechanical loss, control loss, *etc.*. The total iron loss is related with the rotor speed and air gap flux density. As the air gap flux density generated by PMs mounted on the mover inner surface is hardly affected by the armature reaction, the iron loss is only related with the rotary or linear speed.

Fig. 7 shows the iron loss and copper loss of ORVM. It is noticed that the copper loss is increased with the increase of radius, and the iron loss is increased with the increase of axial length. Fig. 8 reveals the power, efficiency and volume contour plots related with the outer radius and axial length of ORVM.



**Fig. 8** Power, efficiency and volume contour plots related with the outer diameter and axial length of ORVM. **a** Power (*W*), **b** efficiency, **c** volume (mm³).



**Fig. 9** The amplitudes of cogging torque related with the the main structural parameters. **a** cogging torque related with $R_{sp2}$, $R_{sp3}$, $w_{pm\theta}$, **b** cogging torque related with $w_{sp4}$, $w_{sp\theta}$

and $w_{sp5}$, **c** magnetic flux density distribution in rotary unit, **d** flux density in regions $A_t$ and $B_p$.

The selected parameter values in Fig. 3 can be divided into two parts: the constant part and changing part. The constant values of $R_{sp2}$, $R_{sp3}$, $w_{pm\theta}$, $w_{sp4}$, $w_{sp\theta}$ and $w_{sp5}$ are 38 mm, 34 mm, 20 mm, 18 mm, 5 mm, and 9 mm, respectively. Figs. 9 (a) and (b) describe the maximum value waveforms of cogging torque related with the change of the main structural parameters. Since the results cannot reflect the mutual influence on electromagnetic characteristics by only changing a single parameter, then the changing ranges of $R_{sp2}$, $R_{sp3}$, $w_{pm\theta}$, $w_{sp4}$, $w_{sp\theta}$ and $w_{sp5}$ are decided as (0.1 mm-0.2 mm, 0.5 mm-0.8 mm), (0.5 mm-1 mm), (0.2 mm-0.4 mm, 0.5 mm-0.8 mm), (0.4 mm-0.5 mm), (1 mm-1.2 mm) and (0.2 mm-0.6 mm, 0.8 mm-1.2 mm), respectively. Fig. 9(c) shows the magnetic flux density distribution in rotary unit. It is noticed that the regions $A_t$ and $B_p$ may have magnetic saturation. And the flux density in regions $A_t$ and $B_p$ are shown in Fig. 9(d), which can be used to decide the $R_{sp3}$ and $w_{sp\theta}$. In order to avoid magnetic saturation of $A_t$, a semicircular structure is added in the stator pole of rotary unit without adding the cogging torque, which is shown in Fig. 10.
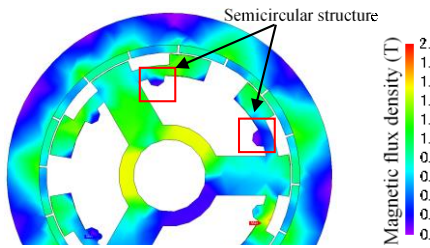


Fig. 10. The flux density distribution of rotary unit.

Fig. 11 exhibits the torque and torque ripple under different current values with different stator yoke heights. It is shown that when $R_{mo}>=53$ mm, $I$=10 A, the average torque can reach the maximum value, and the torque ripple can reach the minimum value.
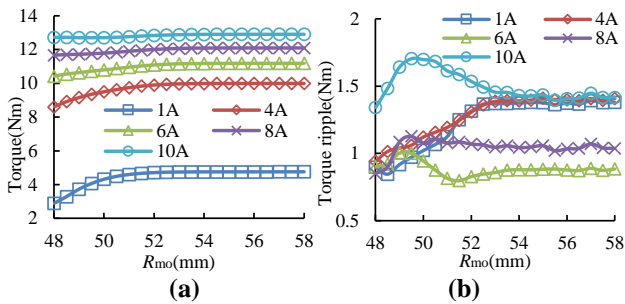


**Fig. 11** Torque outputs under different current values with $R_{mo}$. **a** Average torque, **b** change range of average torque.

Fig. 12 describes the maximum value waveforms of detent force related with the change of the main structural parameters. Since the results cannot reflect the mutual influence on electromagnetic characteristics by only changing a single parameter, then the changing ranges of

$w_{pmz}$, $w_{spz}$, and $w_{sz}$ are decided as (0.2 mm-0.5 mm), (0 mm-0.9 mm) and (0.7 mm-0.9 mm), respectively. The change ranges of $R_{sliz2}$, $R_{sloz1}$, $R_{slz}$ and $R_{sliz1}$ are decided as (0.1 mm-0.3 mm, 0.5 mm-0.7 mm), (0.4 mm-0.6 mm) and (0.4 mm-0.7 mm), respectively.
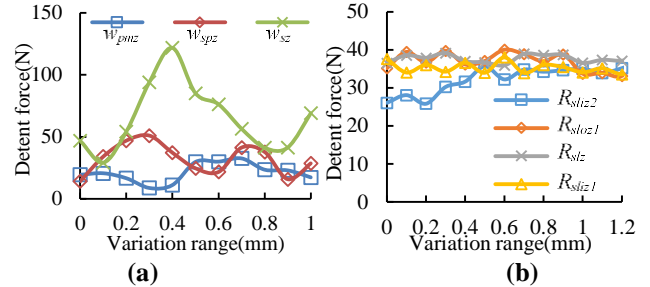


**Fig. 12** The amplitudes of detent force related with the change of the main structural parameters. **a** Detent force related with $w_{pmz}$, $w_{spz}$, and $w_{sz}$, **b** detent force related with $R_{sliz2}$, $R_{sloz1}$, $R_{slz}$ and $R_{sliz1}$.
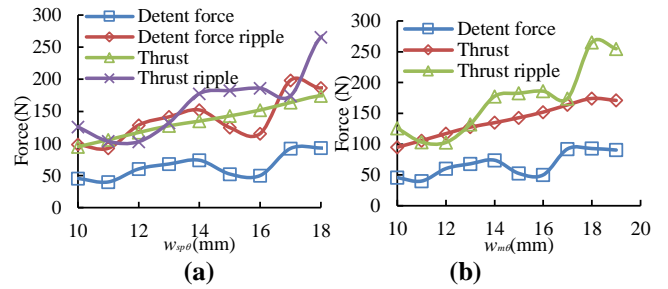


**Fig. 13** Thrust and detent forces related with $w_{sp\theta}$ and $w_{m\theta}$. **a** $w_{sp\theta}$, **b** $w_{m\theta}$.
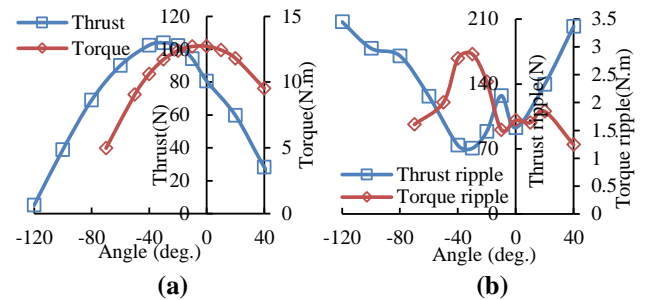


**Fig. 14** Thrust, torque, thrust and torque ripples with different current angles under rated phase currents. **a** Thrust and torque, **b** thrust and torque ripples.

Fig. 13 shows the thrust and detent force related with $w_{sp\theta}$ and $w_{pm\theta}$. It is seen that the change ranges of $w_{sp\theta}$ and $w_{pm\theta}$ are decided as (10 mm, 12 mm) and (14 mm, 17 mm) according to different conditions. Fig. 14 shows the thrust, torque, thrust ripple and torque ripple with different current angles under rated phase currents. It is noticed that when the current angle is in the range of -30° to -10°, the thrust and torque can reach the maximum values, and the thrust ripple and torque ripple can reach the minimum values, respectively.

## 4. Stress Calculation of OMLRVM

According to the requirement of the power, the steels, Q235-A and 40Cr are selected as the materials of rotor, support plate and shaft, respectively. The stress situation in the circumferential, radial and axial directions of OMLRVM are analyzed by 3-D FEM. Since Solid95 unit has three directions of freedom, it is taken as the segmentation type. The stress states of Q235-A and steels can be calculated by the maximum shear stress theory. Fig. 15 shows the displacement contour plots of OMLRVM. It is shown that the stator section of rotary unit may produce the maximum displacement when it works at the load condition. The stator section of linear unit can also produce displacement in circumferential direction. Table I lists the main structure parameters of OMLRVM.
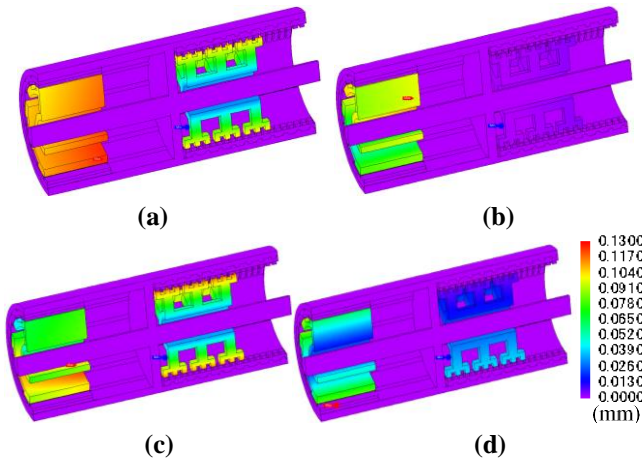


**Fig. 15** Displacement contour plots of OMLRVM. **a** Root mean square, **b** in radial direction, **c** in circumferential direction, **d** in axial direction.

**Table 1** Main parameters of the OMLRVM

| Variables | Value | Variables | Value |
|---|---|---|---|
| $w_{pmz}$(deg.) | 21.5 | $w_{sp}$(mm) | 13.5 |
| $\rho_s$(deg.) | 20 | $R_{mo}$(mm) | 61 |
| $R_{mi}$(mm) | 45 | $R_{sp1}$(mm) | 41.8 |
| $R_{sp2}$(mm) | 38.4 | $R_{sp3}$(mm) | 34.3 |
| $R_{sp4}$(mm) | 18.3 | $w_{m\theta}$(mm) | 11.1 |
| $R_{sp3}$(mm) | 11.4 | $w_{s\theta}$(mm) | 11.4 |
| $w_{mz}$(mm) | 3.85 | $w_{gz}$(mm) | 1.775 |
| $w_{spz}$(mm) | 4.35 | $w_{sppz}$(mm) | 26.1 |
| $w_{sz}$(mm) | 8.7 | $R_{sloz}$(mm) | 41.8 |
| $R_{sloz1}$(mm) | 34.1 | $R_{sloz2}$(mm) | 38.1 |
| $R_{sliz1}$(mm) | 12.7 | $R_{sliz2}$(mm) | 19.7 |
| $N_r$(turns) | 440 | $N_l$(turns) | 150 |

## 5. Electromagnetic Characteristics Analysis

Fig. 16 shows the flux density distribution in OMLRVM. It is noticed that there is no mutual effect between the main magnetic field in rotary unit and that in linear unit.
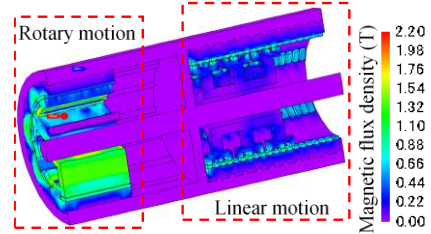


**Fig. 16** Flux density distribution of OMLRVM.

Fig. 17 illustrates air-gap flux density waveforms and their harmonic analyses. It is noticed that the fundamental wave accounts for 71% and 57% of the total harmonics for the rotary and linear units, respectively. Fig. 18 shows the magnetic flux linkage amplitude contour plots, and Fig. 19 shows the torque, thrust, torque change range and thrust change range when the machine works with different current amplitudes and speeds. It is noticed that when the speed of the rotary motion is 450 r/min and the speed of the linear motion is 4 mm/s, the best performance can be obtained. The average torque and average thrust are 12.9 Nm and 70 N, respectively.
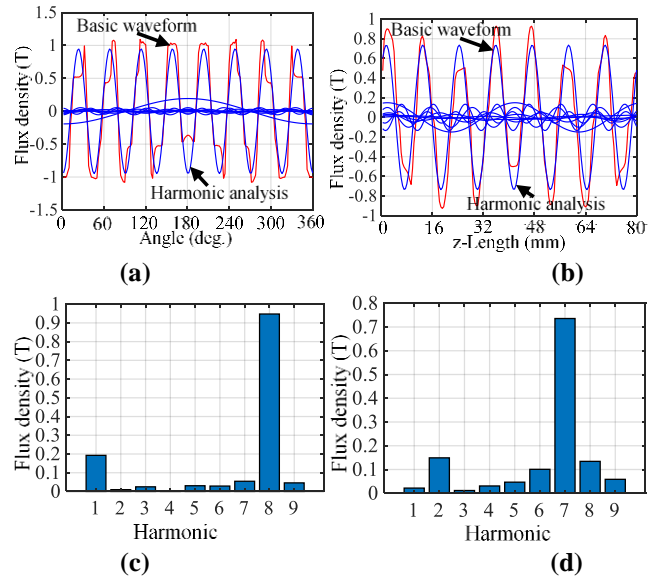


**Fig. 17** Air-gap flux density waveforms and their harmonic analyses. **a** ORVM, **b** OMLVM, **c** air-gap flux density harmonic analysis of ORVM, **d** air-gap flux density harmonic analysis of ORLVM.
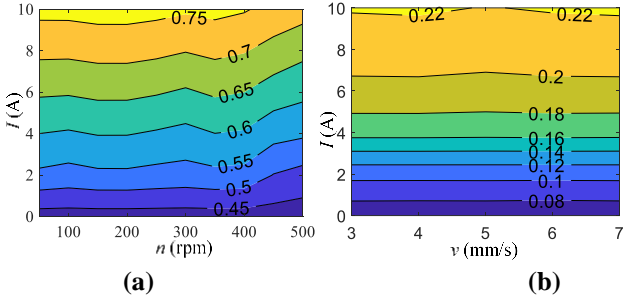
**Fig. 18** Magnetic flux linkage waveforms under different currents and speeds. **a** Phase A, **b** phase D.
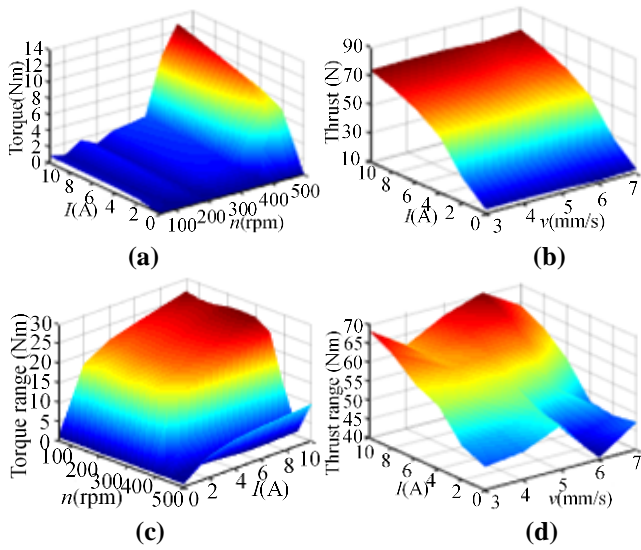


**Fig. 19** Electromagnetic characteristics related with different currents and speeds. **a** Torque, **b** thrust, **c** torque range, **d** thrust range.
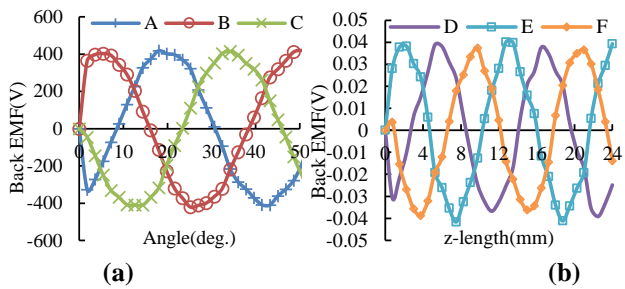


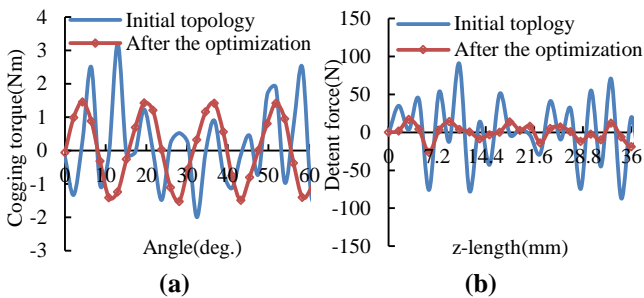**Fig. 20** Back EMF waveforms. **a** ORVM, **b** OMLVM.



**Fig. 21** Waveform comparison of cogging torque and detent force. **a** Cogging torque, **b** detent force.

Fig. 20 exhibits the back EMF waveforms of rotary and linear motion units. The waveforms of the back EMF are more sinusoidal after optimization. Figs. 21 and 22 show the waveform comparison of cogging torque and detent force and their harmonic analyses. It is seen that the amplitudes of cogging torque and detent force are reduced by 54.4% and 80.7%, respectively, compared to those of the initial topology II.
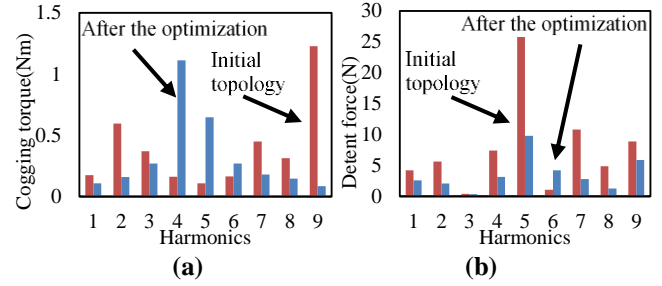


**Fig. 22** Harmonic analysis. **a** Cogging torque, **b** detent force.

## 6. Conclusions

In order to improve the drilling efficiency and precision of drilling robot, an OMLRVM is proposed with a support mechanism. The ORVM is adopted in the rotary unit, which can meet the requirement of the practical application, and the torque can be flexibly adjusted by changing the radial and axial dimensions. The modular stator sections and PM poles of the linear unit are adopted instead of traditional toroid structure to reduce the amplitude of detent force significantly, which can improve the control accuracy and meet the requirement of high precision of linear displacement. The electromagnetic and mechanical parameter optimization designs of the proposed machine are calculated by 3-D FEM. Compared with the results of topology I, the proposed machine can reduce the end effect and electromagnetic coupling effect. It is an effective method to solve the practical engineering problem of drilling motor by the combined method of electromagnetic and mechanical structural designs.

## References

[1] A. A. Almoraya, N. J. Baker, K. J. Smith, M. A. H. Raihan (2019) Design and analysis of a flux-concentrated linear vernier hybrid machine with consequent poles. *IEEE Trans. Ind. Appl.*, 55(5): 4595-4604.

[2] W. Zhao, T. Yao, L. Xu, X. Chen, X. Song (2020) Multi-objective optimization design of a modular linear permanent-magnet vernier machine by combined approximation models and differential evolution. *IEEE Trans. Ind. Electron.*, 66(8): 4634-4645.

[3] D. Cao, W. Zhao, J. Ji, L. Ding, J. Zheng (2019) A generalized equivalent magnetic network modeling method for vehicular dual-permanent-magnet vernier machines. *IEEE Trans. Energy Convers*., 34(4): 1950-1962.

[4] Z. Song, C. Liu, F. Chai, H. Zhao (2020) Modular design of an efficient permanent magnet vernier machine. *IEEE Trans. Magn.*, 56(2):1-6 (**art. 7506406**).

[5] G. Liu, H. Zhong, L. Xu, W. Zhao (2021) Analysis and evaluation of a linear primary permanent magnet vernier machine with multiharmonics. *IEEE Trans. Ind. Electron*., 68(3): 1982-1993.

[6] C. Shi, R. Qu, D. Li, X. Ren, Y. Gao, Z. Chen (2020) Analysis of the fractional pole-pair linear PM vernier machine for force ripple reduction. *IEEE Trans. Ind. Electron*., 68(6):4748-4759.

[7] X. Zhao, S. Niu, X. Zhang, W. Fu (2020) A new relieving-DC-saturation hybrid excitation vernier machine for HEV starter generator application. *IEEE Trans. Ind. Electron.*, 67(8): 6342-6353.

[8] A. Allahyari, H. Torkaman (2020) A novel high-performance consequent pole dual rotor permanent magnet vernier machine. *IEEE Trans. Energy Convers.*, 35(3): 1238-1246.

[9] D. K. Kana Padinharu, G. J. Li, Z. Q. Zhu, M. P. Foster, D. A. Stone, A. Griffo, R. Clark, A. Thomas (2020) Scaling effect on electromagnetic performance of surface-mounted permanent-magnet vernier machine. *IEEE Trans. Magn*., 56(5): 1-15.

[10] W. Wang, M. Cheng, X. Li, M. Tong, J. Qi (2021) Nonlinear analytical solution of magnetic field and performances of a spoke array vernier permanent magnet machine. *IEEE Trans. Energy Convers.,* 36(1): 173-185.

[11] C. Shi, R. Qu, D. Li, X. Ren, Y. Gao, Z. Chen (2021) Analysis of the fractional pole-pair linear PM vernier machine for force ripple reduction. *IEEE Trans. Ind. Electron*., 68(6): 4748-4759.

[12] K. Du, L. Xu, W. Zhao, G. Liu (2021) Analysis and design of a fault-tolerant permanent magnet vernier machine with improved power factor. *IEEE Trans. Ind. Electron*., early access.

[13] Z. Li, Z. Yu, W. Kong, R. Qu, D. Li (2021) An accurate harmonic current suppression strategy for DC-biased vernier reluctance machines based on adaptive notch filter. *IEEE Trans. Ind. Electron*., early access.

[14] L. Fang, D. Li, X. Ren, R. Qu (2021) A novel permanent magnet vernier machine with coding-shaped tooth. *IEEE Trans. Ind. Electron*., early access.

[15] X. Zhao, S. Wang, S. Niu, W. Fu, X. Zhang (2021) A novel high-order-harmonic winding design method for vernier reluctance machine with DC coils across two stator teeth. *IEEE Trans. Ind. Electron*., early access.

[16] L. Wei, T. Nakamura (2021) A novel dual-stator hybrid excited permanent magnet vernier machine with Halbach-array PMs. *IEEE Trans. Magn.*, 57(2): 1-5 (**art. 8101705**).

[17] S. Jia, Y. Liang, D. Liang, J. Liu (2021) A novel DC-biased phase current-independent drive high-speed vernier reluctance machine. *IEEE Trans. Magn.*, 57(6): 1-5 (**art. 8104905**).

[18] Y. Zhou, C. Shi, R. Qu, D. Li, Y. Gao, R. Li (2021) A novel consequent-pole modular-mover linear permanent magnet vernier machine for thrust ripple and cost reduction. *IEEE Trans. Ind. Appl.*, early access.

[19] B. Xu, L. Wu, J. Ma, P. D. Pfister, X. Huang, L. Qiu, Y. Fang, A novel axially magnetized vernier permanent-magnet machine. *IEEE Trans. Magn.*, 57(2): 1-5 (**art. 8101605**).

[20] Y. Zhu, G. Liu, L. Xu, W. Zhao, D. Cao (2021) A hybrid analytical model for permanent magnet vernier machines considering saturation effect. *IEEE Trans. Ind. Electron*., early access.

[21] Y. Zhang, D. Li, P. Yan, X. Ren, R. Qu, J. Ma (2021) A high torque density claw pole permanent-magnets vernier machine. *IEEE J. Emerg. Sel. Topics Power Electron.*, early access.

[22] P. Jin, H. Lin, S. Fang, S. L. Ho (2012) Decoupling control of linear and rotary permanent magnet actuator using two-directional *d-q* transformation. *IEEE Trans. Magn.*, 48(10): 2585-2591.

[23] K. Guo, S. Fang, H. Yang, H. Lin, S. L. Ho (2015) A novel linear-rotary permanent-magnet actuator using interlaced poles. *IEEE Trans. Magn.*, 51(11):1-4 (**art. 8207004**).

[24] P. Bolognesi, O. Bruno, F. Papini, V. Biagini and L. Taponecco (2010) A low-complexity rotary-linear motor useable for actuation of active wheels. In: Proceedings of 2010 International Symposium on Power Electronics, Electrical Drives, Automation and Motion, Jun 2010, pp 331-338.

[25] L. Szabó, I. Benţia and M. Ruba (2012) A rotary-linear switched reluctance motor for automotive applications. In: Proceedings of 2012 International Conference on Electrical Machines, Sept 2012, pp 2615-2621.

[26] F. Xing, B. I. Kwon (2020) Design of a rotary-linear motor with unipolar SPM and voice coil structure. *IEEE Access*, 8: 150291-150300.

[27] S. M. Mirić, R. V. Giuffrida, D. Bortis, J. W. Kolar (2020) Enhanced complex space vector modeling and control system design of multiphase magnetically levitated rotary-linear machines. *IEEE J. Emerg. Sel. Topics Power Electron.*, 8(2): 1833-1849.

[28] O. Safdarzadeh, A. Mahmoudi, E. Afjei, H. Torkaman (2019) Rotary-linear switched reluctance motor: analytical and finite-element modeling. *IEEE Trans. Magn.*, 55(5): 1-10 (**art. 8200710**).

[29] T. J. Teo, H. Zhu, S. Chen, G. Yang, C. K. Pang (2016) Principle and modeling of a novel moving coil linear-rotary electromagnetic actuator. *IEEE Trans. Ind. Electron*., 63(11): 6930-6940.

[30] L. Xu, X. Zhu, C. Zhang, L. Zhang, L. Quan (2021) Power oriented design and optimization of dual stator linear-rotary generator with Halbach PM array for

ocean energy conversion. *IEEE Trans. Energy Convers*., early access.

[31] L. Xie, J. Si, T. -F. Wu, Y. Hu, J. Zhou, S. Xu (2021) Analysis and suppression techniques of helical motion coupling effect for the 2DoF direct drive induction machine. *IEEE Trans. Ind. Electron*., early access.

[32] K. Guo, Y. Guo (2021) Design optimization of linear-rotary motion permanent magnet generator With E-shaped stator," *IEEE Trans. Appl. Supercond.*, 31(8): 1-5 (**art. 0600705**).